



Article

Fractal-Based Approaches to Pore Structure Investigation and Water Saturation Prediction from NMR Measurements: A Case Study of the Gas-Bearing Tight Sandstone Reservoir in Nanpu Sag

Weibiao Xie ^{1,2,*}, Qiuli Yin ^{1,2,*}, Jingbo Zeng ³, Guiwen Wang ^{2,4}, Cheng Feng ^{1,2} and Pan Zhang ^{1,2}

¹ School of Petroleum, China University of Petroleum (Beijing) at Karamay, 355 Anding Road, Karamay 834000, China

² State Key Laboratory of Petroleum Resources and Prospecting, China University of Petroleum (Beijing), Beijing 102249, China

³ China Petroleum Logging Co., Ltd., Xi'an 710000, China

⁴ College of Geosciences, China University of Petroleum (Beijing), Beijing 102249, China

* Correspondence: gareth123@126.com (W.X.); 2022592107@cupk.edu.cn (Q.Y.); Tel.: +86-15932597520 (W.X.); +86-15832597520 (Q.Y.)

Abstract: Pore space of tight sandstone samples exhibits fractal characteristics. Nuclear magnetic resonance is an effective method for pore size characterization. This paper focuses on fractal characteristics of pore size from nuclear magnetic resonance (NMR) of tight sandstone samples. The relationship between the fractal dimension from NMR with pore structure and water saturation is parameterized by analyzing experimental data. Based on it, a pore structure characterization and classification method for water-saturated tight sandstone and a water saturation prediction method in a gas-bearing sandstone reservoir have been proposed. To verify the models, the fractal dimension from NMR of 19 tight sandstone samples selected from the gas-bearing tight sandstone reservoir of Shahejie Formation in Nanpu Sag and that of 16 of them under different water saturation states are analyzed. The application result of new methods in the gas-bearing tight sandstone reservoir of Shahejie Formation in Nanpu Sag shows consistency with experimental data. This paper has facilitated the development of the NMR application by providing a non-electrical logging idea in reservoir quality evaluation and water saturation prediction. It provides a valuable scientific resource for reservoir engineering and petrophysics of unconventional reservoir types, such as tight sandstone, low porosity, and low permeability sandstone, shale, and carbonate rock reservoirs.

Keywords: fractal dimension; pore structure; water saturation; NMR



Citation: Xie, W.; Yin, Q.; Zeng, J.; Wang, G.; Feng, C.; Zhang, P. Fractal-Based Approaches to Pore Structure Investigation and Water Saturation Prediction from NMR Measurements: A Case Study of the Gas-Bearing Tight Sandstone Reservoir in Nanpu Sag. *Fractal Fract.* **2023**, *7*, 273. <https://doi.org/10.3390/fractalfract7030273>

Academic Editors: Carlo Cattani, Jordan Hristov and Zine El Abidine Fellah

Received: 9 January 2023

Revised: 22 February 2023

Accepted: 17 March 2023

Published: 21 March 2023



Copyright: © 2023 by the authors. Licensee MDPI, Basel, Switzerland. This article is an open access article distributed under the terms and conditions of the Creative Commons Attribution (CC BY) license (<https://creativecommons.org/licenses/by/4.0/>).

1. Introduction

Gas-bearing tight sandstone reservoir is a hot field of energy exploration and development [1]. It is an important part of unconventional oil and gas reservoirs and has attracted substantial attention from experts and scholars of reservoir, geology, petrophysical, and other fields [2,3]. Strong pore structure heterogeneity leads to difficulties in reservoir evaluation of flow capacity, seepage characteristics, and gas production prediction [4–6].

Since the fractal theory was introduced by Mandelbrot [7], it has been widely applied in pore structure characterization and pore fluid flow investigation associated with porous media [8–10]. Li K. et al. described pore structure heterogeneity by means of fractal theory [11,12]. Wang Q. et al. derived a fractal-based permeability model for shale and sandstone and compared its accuracy with common permeability models [13,14]. Song Z. et al. presented evidence that the pore space of tight sandstone is fractal, and the fractal dimension is a function of pore size [15,16]. Rembert et al. studied the electrical characteristics of rock by means of fractal theory and determined the relationship between

fractal dimension and Archie model coefficients [17,18]. Shi Y. et al. established a model for rock resistivity with relative permeability from fractal dimension [19]. Karimpouli et al. simulated petro physically digital cores through fractal theory, and the result can meet the expected requirements [20,21].

As the pore space of sandstone samples has been proven to exhibit fractal properties, a growing interest is raised in applying fractal characteristics of pore space to reservoir evaluation. Especially, fractal dimensions of pore space have been studied extensively [22] and mainly applied in the analysis of pore structure [23]. Nuclear magnetic resonance (NMR) T_2 spectra provide measurements of pore space distribution [24–26]. However, reports about applying fractal dimensions from NMR in pore structure characterization and water saturation prediction of tight sandstone are rare.

This paper studies the relationship of fractal dimensions from NMR with pore structure parameters and water saturation of gas-bearing tight sandstone. According to double fractal theory and T_{2cut} value, the fractal dimension from NMR, including the fractal dimension of the macro-pore system D_{va} and that of the micro-pore system D_{vb} , is derived. 19 tight sandstone samples selected from the gas-bearing tight sandstone reservoir of Shahejie Formation in Nanpu Sag have proved that for rock samples with similar pore structure (showing similar T_2 spectra monography), their D_{va} and D_{vb} values are centralized within specific ranges and are independent of porosity. Additionally, D_{va} is in direct ratio to T_{2lm} and S_{wir} , but D_{vb} has no obvious correlation with these two parameters. In addition, 16 of the samples under different water saturation have revealed decreasing S_w versus increasing D_{va} , but D_{vb} has little variation, and ΔD_{va} (the increment of D_{va}) is directly related to the water saturation. Based on the above, a pore structure characterization and classification method for water-saturated tight sandstone and a water saturation prediction method in a gas-bearing tight sandstone reservoir have been proposed. The application result of new methods in the gas-bearing tight sandstone reservoir of Shahejie Formation in Nanpu Sag shows consistency with experimental data. Thus, the fractal dimension from NMR can be used in pore structure characterization, classification, and water saturation prediction, providing a non-electrical idea for the qualitative identification and evaluation of gas-bearing tight sandstone reservoirs. It has a reference and guiding significance for the gas-bearing recognition of other types of reservoirs.

2. Methodology

2.1. Pore Structure Investigation of Water-Saturated Tight Sandstone Based on Fractal Analysis from NMR Spectra

As claimed by some researchers, pore space in clastic rock has exhibited a certain degree of self-similarity [16], indicating that the fractal theory can be used to predict the distribution property of pore size. By means of fractal geometry, the following model for pore space distribution in clastic rock has been proposed [27]:

$$S = \left(\frac{r}{r_{max}} \right)^{3-D_r} \quad (1)$$

where r (μm) is the pore radius; r_{max} (μm) is the maximum radius of pores; S (%) is the volume ratio of pores whose pore radius is within the range from 0 to r ; D_r (none) is the fractal dimension of pore size, generally $0 < D_r < 3$. In Equation (1), S is related to measured scale r through fractal dimension D_r .

According to NMR relaxation principle, pore fluids in sandstone involve three relaxation mechanisms: surface relaxation; bulk relaxation; and diffusion relaxation. As bulk relaxation time and diffusion relaxation time of water-saturated rock samples can be ignored, the relationship between surface relaxation and pore size in water-saturated rock is

$$\frac{1}{T_2} = \rho \left(\frac{S}{V} \right) = F_s \frac{\rho}{r} \quad (2)$$

where T_2 (ms) is the surface relaxation time; ρ ($\mu\text{m}/\text{ms}$) is the surface relaxivity (i.e., T_2 relaxing strength of the grain surfaces); F_s (none) is the pore geometry factor; S (μm^2) is the pore surface area; and V (μm^3) is the pore volume. Moreover, (S/V) , the ratio of pore surface to fluid volume, is a measure of pore size.

Bringing Equation (2) into Equation (1) obtains

$$S_v = \left(\frac{T_{2max}}{T_2} \right)^{D_v-3} \quad (3)$$

where S_v (%) is the volume ratio of pores whose surface relaxation are within the range from 0 to T_2 ; T_{2max} (ms) is the maximum surface relaxation time of pores; D_v (none) is the fractal dimension of pore size determined by NMR T_2 spectra curve.

A lot of works have reported that the pore space of the rock has multi-dimensional fractal features [16]. For the mobility of reservoir fluids being primarily controlled by pore space, pore water in tight sandstone can be grouped into movable water and immovable water according to flow capacity. T_2 value relates directly to pore size in water-saturated rock. Assuming movable water is mainly held in a macro-pore system, which has responses of big T_2 value, and immovable water resides in a micro-pore system, corresponding to small T_2 value, NMR T_{2cut} value can be used as an inflection point to divide the NMR T_2 spectral curve into two segments. By means of a double fractal method [28], the D_v is given by

$$D_v = \begin{cases} D_{va}, T_2 \in [T_{2cut}, T_{2max}] \\ D_{vb}, T_2 \in [T_{2min}, T_{2cut}] \end{cases} \quad (4)$$

where T_{2cut} (ms) is a fixed T_2 value separating movable fluids occupied macro-pores and immovable fluids occupied micro-pores; T_{2min} (ms) is the minimum transverse relaxation time of pores; D_{va} and D_{vb} are fractal dimensions of the macro-pore system and micro-pore system from NMR, respectively.

Then, Equation (3) is rewritten as

$$\text{Log}_{10}(S_v) = \begin{cases} (D_{va} - 3)[\text{Log}_{10}(T_{2max}) - \text{Log}_{10}(T_2)], T_2 \in [T_{2cut}, T_{2max}] \\ (D_{vb} - 3)[\text{Log}_{10}(T_{2max}) - \text{Log}_{10}(T_2)], T_2 \in [T_{2min}, T_{2cut}] \end{cases} \quad (5)$$

Equation (5) is the fractal model for pore size distribution in water saturated tight sandstone reservoirs studied from NMR measurements. It has shown a piecewise linear relationship between $\text{Log}_{10}S_v$ and $\text{Log}_{10}T_2$, and line slopes of macro-pore and micro-pore systems are directly related to their fractal dimensions from NMR, respectively indicating that fractal dimensions from NMR are corresponding to pore space heterogeneity and can be used to characterize pore structure.

2.2. Water Saturation Prediction Method of Gas-Bearing Tight Sandstone Based on Fractal Analysis from NMR Spectra

Based on Equation (3), the NMR-based fractal model of water-saturated rock is

$$S_{v,0} = \left(\frac{T_{2max,0}}{T_2} \right)^{D_{v,0}-3} \quad (6)$$

where, $S_{v,0}$ (%) is the volume ratio of pores, whose surface relaxation is within the range from 0 to T_2 ; $T_{2max,0}$ (ms) is the maximum surface relaxation time of pores; $D_{v,0}$ (none) is the fractal dimension of pore size from NMR. NMR-measured porosity of water saturated rock is ϕ_0 , it is approximately equal to total porosity of the rock sample. $T_{2max,0}$ is the NMR response of the maximum pore.

In gas-bearing sandstone reservoirs, NMR measurements mainly respond to the presence of hydrogen protons in water because the gas signal is difficult to be captured due to its rapid diffusion. As a result, the signal of pores filling with gas is lost by NMR measurements. In Figure 1, pores of different sizes are simplified as circles with different

diameters, water is shown in blue, and gas is colored yellow. The pore size distribution of the water-saturated rock sample (as shown in Figure 1A) satisfies Equation (6). When the maximum pore is filling with gas (as shown in Figure 1B), the NMR response of gas-filling pores is ignorable, the pore size distribution of the equivalent rock (as shown in Figure 1E) satisfies

$$S_{v,1} = \left(\frac{T_{2max,1}}{T_2} \right)^{D_{v,1}-3} \quad (7)$$

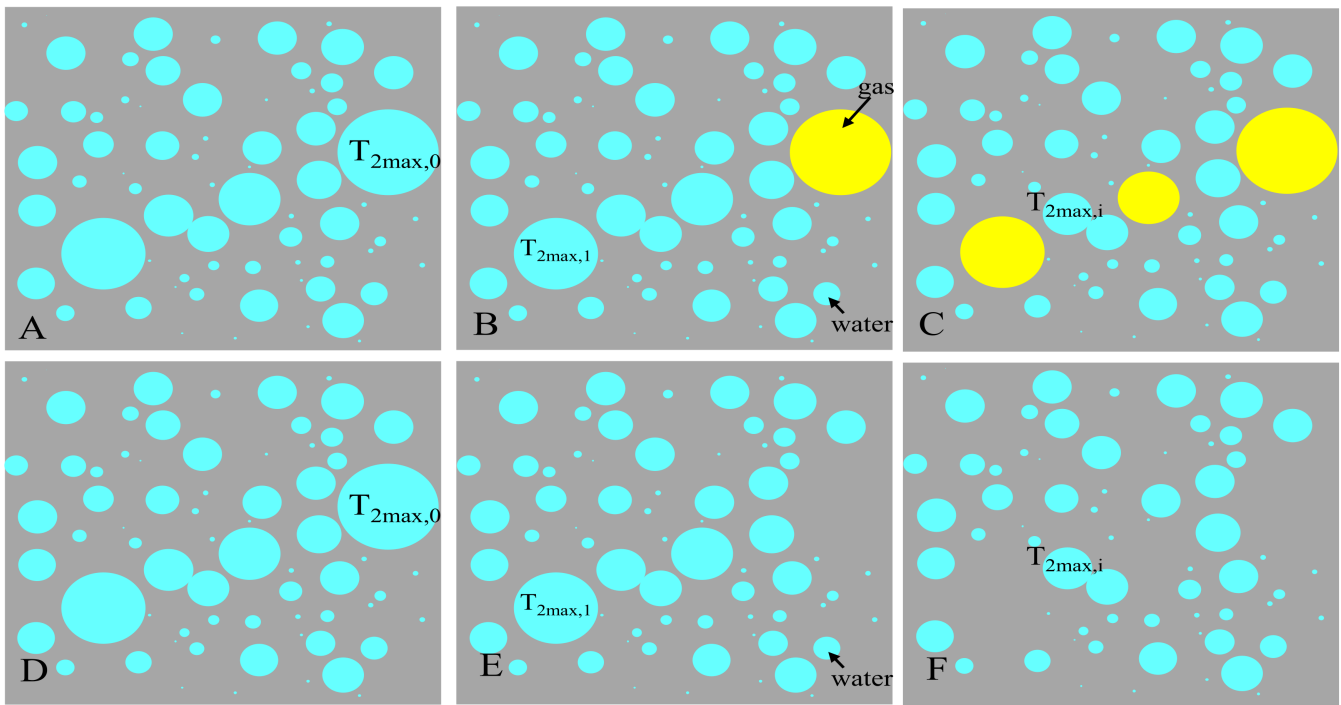


Figure 1. Influence of gas filling on pore structure from NMR. (A) Water-saturated rock; (D) Equivalent pore structure model of (A) from NMR; (B) The maximum pore in (A) is filling with gas; (E) Equivalent pore structure model of (B) from NMR; (C) Gas filling in the pores bigger than the $(i - 1)$ -th largest pore; (F) Equivalent pore structure model of (C) from NMR.

In Equation (7), $S_{v,1}$ (%) is the volume ratio of pores, whose surface relaxation is within the range from 0 to T_2 . $T_{2max,1}$ (ms) is the maximum surface relaxation time of pores of the equivalent rock shown in Figure 1E. ϕ_1 is approximately equal to total porosity minus the porosity of the gas-filled pore. $D_{v,1}$ is the fractal dimension from NMR.

Gas, as a non-wetting phase, preferentially enters into macro-pores, it continuously enters into the pore space from macro- to micro-pores with the increase in pressure. In this way, pores filling with gas are unable to be detected by NMR when the i -th largest pore is filling with gas, as shown in Figure 1C, its pore structure model from NMR is shown in Figure 1F. NMR measured porosity is ϕ_i and the maximum surface relaxation time of pores is $T_{2max,i}$. The pore size distribution of the equivalent rock satisfies the following two equations:

$$S_{v,i} = \left(\frac{T_{2max,i}}{T_2} \right)^{D_{v,i}-3} \quad (8)$$

$$\text{Log}_{10}(S_{v,i}) = (D_{v,i} - 3)[\text{Log}_{10}(T_{2max,i}) - \text{Log}_{10}(T_2)] \quad (9)$$

In Equation (9), it can be seen that the fractal dimension from NMR $D_{v,i}$ is a function of both water saturation (it can be calculated by ϕ_i/ϕ_0 as the sum of gas filling porosity and water occupied porosity is 1 in as-bearing sandstone reservoirs) and pore size distribution.

Further, using function f to express the relationship between water saturation and fractal dimension variation $\Delta D_v (= D_{v,i} - D_{v,0})$,

$$\Delta D_v = D_{v,i} - D_{v,0} = f(S_w) \quad (10)$$

Then, Equation (8) is given as

$$S_{v,i} = \left(\frac{T_{2max,i}}{T_2} \right)^{f(S_w) + D_{v,0} - 3} \quad (11)$$

Equation (11) shows the relationship between the fractal dimension from NMR and water saturation in gas-bearing tight sandstone reservoirs. It is the fractal-based method of water saturation prediction in gas-bearing sandstone reservoirs from NMR data.

3. Model Validation

In this research, a total of 19 tight sandstone samples collected from five boreholes are selected from the gas-bearing tight sandstone reservoir of Shahejie Formation in Nanpu Sag. The sandstone has undergone strong compaction and cementation; it is featured with low porosity, low permeability, and strong pore structure heterogeneity. Its location near Shahejie source rock in Nanpu depression makes it one of the most important gas potential areas in east China. More details of geological settings are available in previous studies [29–31]. Testing includes two procedures. Firstly, all samples are tested and analyzed for physical properties. Secondly, NMR experiments of samples under different water saturations are performed. All samples are shaped into cylinders with a diameter of 2.5 cm and a length of 4.9 (± 0.2) cm, washed with dichloromethane and distilled water, and then dried. Porosity is determined by the Porem-200 instrument (Core Lab Corporation, Houston, TX, USA) through helium injection, and permeability is measured by the STY-2 gas permeability tester by using helium as the carrier gas. Irreducible water saturation S_{wir} is determined using a centrifuge of 150 psi pressure. T_2 spectra under different water saturation states (the samples are firstly water-saturated and then centrifuged with different speeds) are measured by MARAN-II equipment operated at 35 °C; the resonance frequency is 2 MHz, the waiting time is 6000 ms, and echo spacing is 0.2 ms; the number of scans is 128. T_{2cut} is determined by comparing T_2 spectra obtained on fully and partially water-saturated core samples. T_{2lm} is the geometrical mean of the relaxation spectra.

Table 1 shows the specific parameters of all 19 samples. Ranges of the measured porosity and permeability are (5.7, 15.3) % and (0.151, 31.125) md, respectively; the average value is 11.21% and 5.62 md. However, as the burial depth is more than 4300 m, the overburden pressure has an obvious influence on reservoir porosity and permeability. According to previous studies [29–31], porosity and permeability under reservoir conditions generally decrease about 20–10% compared with the measured permeability under normal pressure. Thus, these samples belong to tight sandstone.

Table 1. Specific parameters of 19 rock samples.

No.	T ₂ Curves Morphology	Porosity v/v	Permeability md	S _{wir} v/v	T _{2cut} ms	T _{2lm} ms	Dva	Dvb	f ₁ v/v	f ₂ v/v	f ₃ v/v	f ₄ v/v	f ₅ v/v
1	right unimodal pattern (T ₂ value of peak: 200 ms)	12.51	23.21	16.00	14.70	74.67	2.52	1.30	0.61	0.19	0.10	0.05	0.05
2		11.30	8.74	20.78	22.59	70.64	2.56	1.21	0.60	0.18	0.12	0.06	0.04
3		10.90	4.49	25.49	14.85	52.22	2.58	1.45	0.55	0.20	0.12	0.07	0.06
4		13.90	31.13	16.72	19.71	77.62	2.48	1.28	0.64	0.21	0.11	0.03	0.01
5		11.20	7.03	26.21	13.66	44.08	2.59	1.36	0.43	0.27	0.15	0.08	0.07
6		11.30	6.81	26.37	17.43	43.63	2.58	1.46	0.49	0.24	0.14	0.07	0.06
7		12.00	14.49	19.51	16.37	73.55	2.56	1.40	0.61	0.19	0.12	0.05	0.04
	Range average value	<u>10.9–13.9</u> 11.76	<u>4.49–31.13</u> 13.7	<u>16–26.37</u> 21.58	<u>13.66–22.59</u> 17.04	<u>43.63–77.62</u> 62.35	<u>2.48–2.59</u> 2.55	<u>1.21–1.46</u> 1.35	<u>0.43–0.64</u> 0.56	<u>0.18–0.27</u> 0.21	<u>0.1–0.15</u> 0.12	<u>0.03–0.08</u> 0.06	<u>0.01–0.07</u> 0.05
8	balanced bimodal pattern	13.23	1.61	46.11	13.39	17.96	2.80	1.15	0.33	0.15	0.23	0.15	0.14
9		12.20	1.98	49.35	10.90	18.57	2.78	1.19	0.33	0.16	0.20	0.16	0.15
	Range average value	<u>12.2–13.23</u> 12.72	<u>1.61–1.98</u> 1.79	<u>46.11–49.35</u> 47.73	<u>10.9–13.39</u> 12.15	<u>17.96–18.57</u> 18.27	<u>2.78–2.80</u> 2.79	<u>1.15–1.19</u> 1.17	<u>0.33–0.33</u> 0.33	<u>0.15–0.16</u> 0.155	<u>0.2–0.23</u> 0.215	<u>0.15–0.16</u> 0.155	<u>0.14–0.15</u> 0.145
10	right unimodal pattern (T ₂ value of peak: 30 ms)	8.06	0.49	50.52	17.48	15.40	2.70	1.30	0.15	0.31	0.26	0.12	0.17
11		14.10	2.49	44.17	23.98	27.89	2.73	1.54	0.36	0.25	0.21	0.09	0.09
12		14.70	1.00	48.36	19.57	18.85	2.75	1.35	0.31	0.24	0.23	0.10	0.12
13		13.10	0.69	45.92	14.31	16.97	2.76	1.18	0.28	0.25	0.24	0.11	0.13
14		14.80	0.66	55.01	21.27	16.66	2.78	1.45	0.28	0.25	0.23	0.09	0.15
15		15.30	1.09	48.98	16.22	15.40	2.78	1.32	0.25	0.27	0.23	0.10	0.15
	Range average value	<u>8.6–15.3</u> 13.34	<u>0.49–2.49</u> 1.07	<u>44.17–55.01</u> 48.83	<u>14.31–23.98</u> 18.81	<u>15.4–27.89</u> 18.52	<u>2.70–2.78</u> 2.75	<u>1.18–1.54</u> 1.36	<u>0.15–0.36</u> 0.27	<u>0.24–0.31</u> 0.26	<u>0.21–0.26</u> 0.23	<u>0.09–0.12</u> 0.1	<u>0.09–0.17</u> 0.13
16	balanced unimodal pattern (T ₂ value of peak: 10 ms)	5.70	0.31	62.75	18.19	11.67	2.80	1.70	0.17	0.19	0.34	0.15	0.15
17		8.90	0.22	58.64	15.81	11.20	2.85	1.69	0.17	0.22	0.31	0.15	0.15
	Range average value	<u>5.7–8.9</u> 7.3	<u>0.22–0.31</u> 0.27	<u>58.64–62.75</u> 60.7	<u>15.81–18.19</u> 17	<u>11.2–11.67</u> 11.43	<u>2.80–2.85</u> 2.83	<u>1.69–1.70</u> 1.69	<u>0.17–0.17</u> 0.17	<u>0.19–0.22</u> 0.21	<u>0.31–0.34</u> 0.325	<u>0.15–0.15</u> 0.15	<u>0.15–0.15</u> 0.15
18	left bimodal pattern	8.75	0.15	58.72	2.58	2.69	2.89	0.59	0.28	0.05	0.12	0.15	0.41
19		12.50	0.20	54.60	4.52	6.55	2.86	0.89	0.20	0.13	0.17	0.18	0.32
	Range average value	<u>8.75–12.5</u> 10.63	<u>0.15–0.20</u> 0.18	<u>54.6–58.72</u> 56.66	<u>2.58–4.52</u> 3.55	<u>2.69–6.55</u> 4.62	<u>2.86–2.89</u> 2.88	<u>0.59–0.89</u> 0.74	<u>0.2–0.28</u> 0.24	<u>0.05–0.13</u> 0.09	<u>0.12–0.17</u> 0.14	<u>0.15–0.18</u> 0.16	<u>0.41–0.32</u> 0.36

3.1. Pore Structure Characterization Method Based on Fractal Analysis from NMR Spectra

19 samples can be classified into five groups according to NMR T_2 curves morphology, including Type A (no. 1–7, shown in Figure 2A), Type B (no. 8–9, shown in Figure 2B), Type C (no. 10–15, shown in Figure 2C), Type D (no. 16–17, shown in Figure 2D), and Type E (no. 18–19, shown in Figure 2E). Type A is dominant of the right unimodal pattern with a T_2 peak (corresponding T_2 value of the curve peak) of 200 ms, representing a higher proportion of macro-pores; Type B is featured with a balanced bimodal pattern with two T_2 peaks of 100 ms and 3 ms, indicating similar proportions of macro-pores and micro-pores; Type C is characterized by the right unimodal pattern with a T_2 peak of 30 ms; Type D is mainly of unimodal pattern with a T_2 peak of 10 ms, and Type E is left bimodal pattern with a T_2 peak of 1 ms, showing that Type D and Type E are dominantly made of micro-pores. In Table 1, for Type A, B, C, D, and E, the average Swir is 21.58%, 47.73%, 48.83%, 60.7%, and 56.66%, and the average permeability is 13.7 md, 1.79 md, 1.07 md, 0.27 md, and 0.18 md, respectively. It indicates that as the T_2 curve transforms from Type A to Type E, the T_2 peak moves from right to left and corresponds to an increasing micro-pores proportion, increasing Swir and decreasing permeability, indicating that the pore structure becomes more complex.

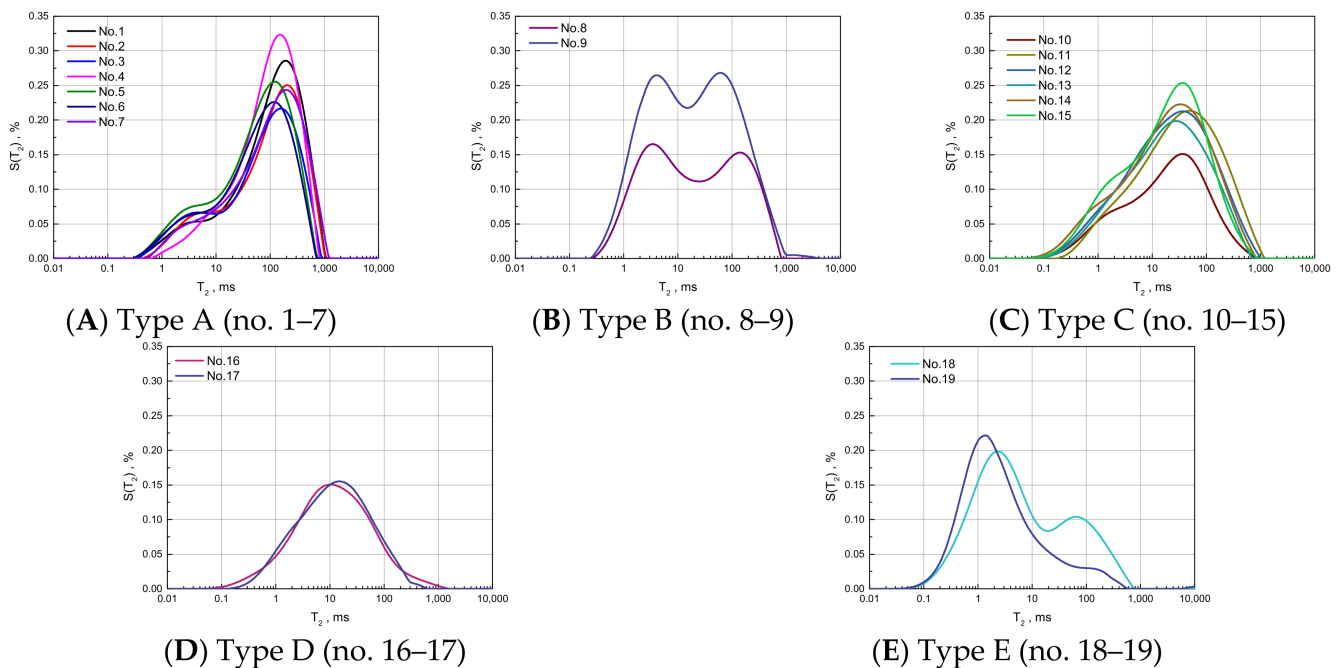


Figure 2. T_2 curves of 19 rock samples and pore structure classification.

Figure 3 shows D_{va} and D_{vb} distribution ranges of Types A–E. D_{va} and D_{vb} are derived from $\text{Log}_{10}S_v - \text{Log}_{10}T_2$ line slopes of the macro-pore system and micro-pore system according to Equation (5). The calculated D_{va} and D_{vb} are listed in Table 1. In Figure 3, D_{va} and D_{vb} distributions are marked in grey and red, respectively. The calculated D_{va} and D_{vb} ranges are [2.48, 2.59] and [1.21, 1.46] for Type A, [2.78, 2.80] and [1.15, 1.19] for Type B, [2.70, 2.78] and [1.18, 1.54] for Type C, [2.80, 2.85] and [1.69, 1.70] for Type D, and [2.80, 2.85] and [1.69, 1.70] for Type E. The result shows that the D_{va} and D_{vb} value of the same rock type, which has similar T_2 curve morphology, although with different porosity, is centrally distributed, indicating that rock samples having similar pore structures have similar fractal dimensions.

Based on the analysis above, a pore structure classification scheme according to D_{va} and D_{vb} is made. In Figure 4, 5 types of pore structure, including Types I, II, III, IV, and V, are grouped on $D_{va} - D_{vb}$ cross plot; they are colored in grey, red, green, purple, and blue, respectively. Type I is within the range of $2.63 \geq D_{va} > 0$ and $3 > D_{vb} \geq 1.2$; it

is characterized by the most favorable petrophysical properties, the permeability higher than 4 md, T_2 curve of right unimodal pattern with a peak of more than 100 ms and low immovable water content. Type II is dominantly distributed within $2.77 \geq D_{va} > 0$ and $1.2 \geq D_{vb} > 0.9$ and $2.85 \geq D_{va} > 2.77$ and $1.5 \geq D_{vb} \geq 1.2$. It usually has good petrophysical properties and is featured by the permeability of between 0.4 md and 4 md, T_2 curve of balanced bimodal pattern, and relatively low immovable water content. Type III mainly occupies the area $2.77 \geq D_{va} > 2.63$ and $3 > D_{vb} \geq 1.2$; it has relatively good petrophysical properties; the permeability is within 0.4–4 md; it is characterized by the T_2 curve of right unimodal pattern with a peak of less than 100 ms and relatively low immovable water content. Type IV is distributed within $2.85 \geq D_{va} > 2.77$ and $3 > D_{vb} > 1.5$; it has poor petrophysical properties; its permeability is less than 0.4 md, and it has T_2 curve of unimodal pattern and relatively high immovable water content. Type V is mainly distributed within $3 > D_{va} > 2.85$ and $0.9 \geq D_{vb} > 0$; it has the poorest petrophysical properties; it has a permeability of less than 0.4 md, T_2 curve of left bimodal pattern and high immovable water content. Further, from 19 rock samples in Figure 4, it can be seen that samples 1–7, marked by black squares, fall into Type I; samples 8–9, marked by red dots, land within Type II; samples 10–15, marked by green triangles, scatter across Type III; rock samples 16–17, marked by purple inverted triangles, belong to Type IV, and samples 18–19, marked by blue diamonds, are classified into Type V. The result indicates that pore structure classification can be achieved based on fractal analysis from NMR spectra.

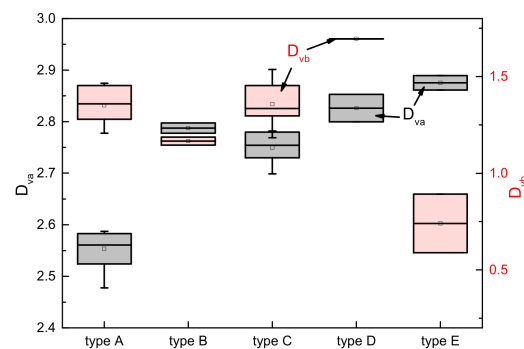


Figure 3. D_{va} and D_{vb} distribution of Type A–E.

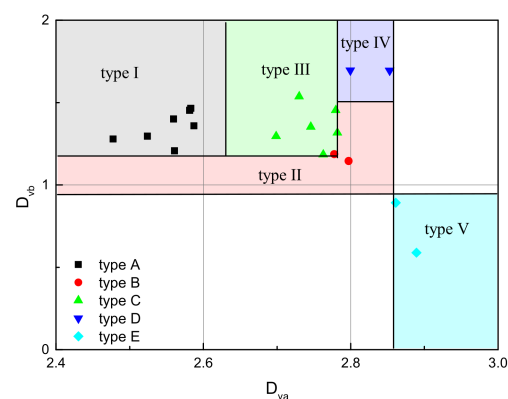
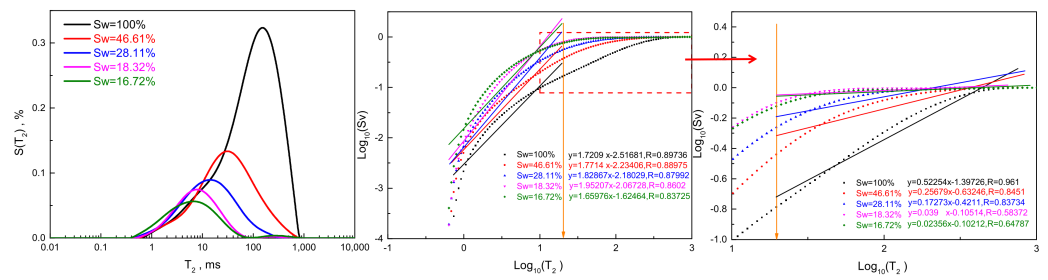


Figure 4. Pore structure classification based on D_{va} – D_{vb} cross plot.

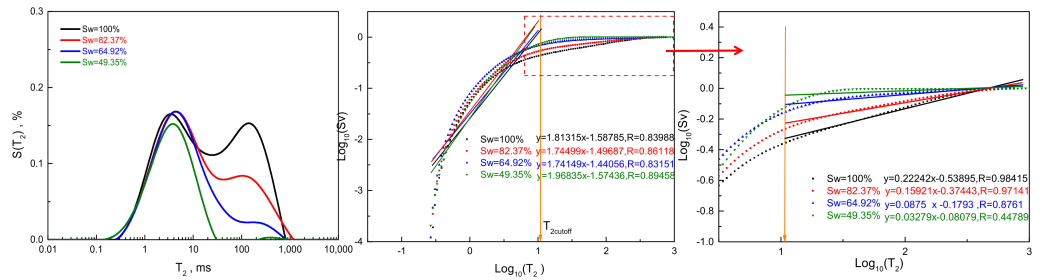
3.2. Water Saturation Prediction Method Based on Fractal Analysis from NMR Spectra

Among 19 rock samples listed in Table 1, T_2 spectra of 16 samples under different water saturation states are obtained, and their specific parameters are listed in Table 2. Figure 5 shows T_2 spectra, cumulative curves, and corresponding fitting models under different water saturation states of a representative rock sample of each pore structure type.

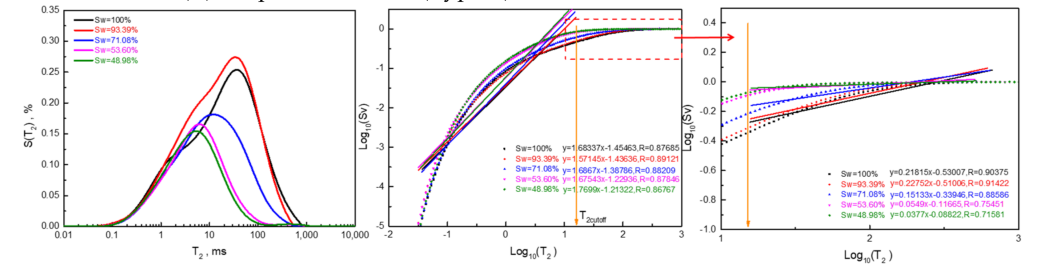
In this section, the pore size is divided into macro-pores and micro-pores according to T_{2cut} .



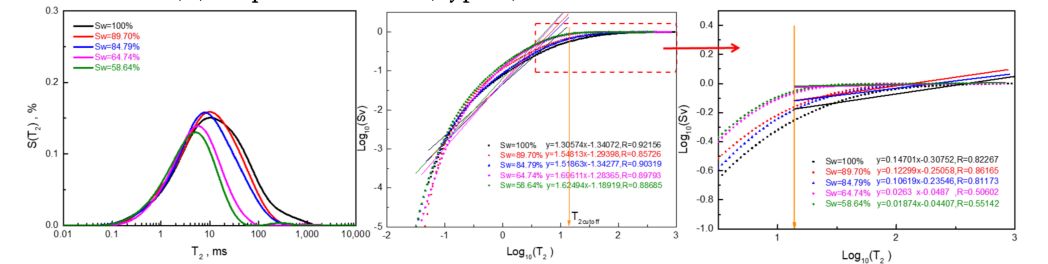
(A) T_2 spectra of No. 4 (Type A) under different water saturation



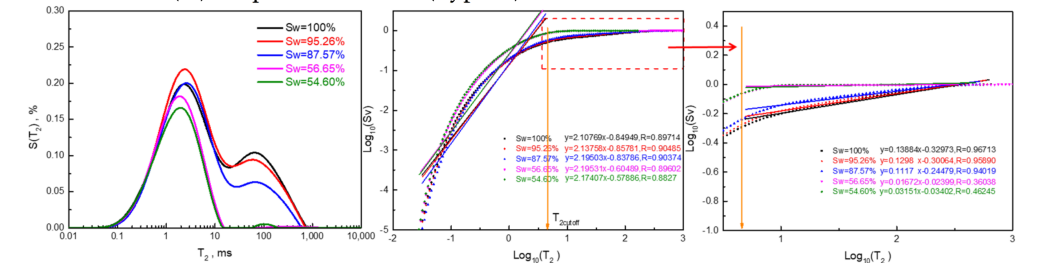
(B) T_2 spectra of No. 9 (Type B) under different water saturation



(C) T_2 spectra of No. 15 (Type C) under different water saturation



(D) T_2 spectra of No. 17 (Type D) under different water saturation



(E) T_2 spectra of No. 19 (Type E) under different water saturation

Figure 5. T_2 spectra under different water saturation states of a representative rock sample of each pore structure type.

Table 2. Fractal dimensions of 16 rock samples under different water saturation states.

No	Sw	T _{2lm}	D _{va}	D _{vb}	ΔD _{va}	No	Sw	T _{2lm}	D _{va}	D _{vb}	ΔD _{va}
1	100.00	74.67	2.52	1.30	0.00	10	100.00	15.40	2.70	1.30	0.00
	48.75	25.88	2.73	1.38	0.21		93.49	13.86	2.70	1.39	0.00
	29.67	10.08	2.81	1.30	0.29		77.48	9.18	2.75	1.24	0.05
	18.56	4.90	2.94	1.38	0.42		54.70	4.90	2.90	1.28	0.20
	16.00	3.60	2.97	1.23	0.44		50.52	4.25	2.93	1.21	0.23
2	100.00	70.64	2.56	1.21	0.00	11	100.00	27.89	2.73	1.54	0.00
	58.08	31.57	2.73	1.38	0.17		89.04	22.11	2.75	1.49	0.02
	34.31	9.82	2.87	1.36	0.31		59.55	9.39	2.86	1.42	0.13
	22.10	6.08	2.94	1.28	0.38		44.17	4.94	2.92	1.38	0.19
	20.78	4.74	2.96	1.15	0.40		100.00	18.85	2.75	1.35	0.00
3	100.00	52.22	2.58	1.45	0.00	12	93.46	17.33	2.77	1.46	0.02
	69.00	38.75	2.68	1.59	0.10		71.52	8.60	2.83	1.27	0.09
	40.66	10.13	2.79	1.28	0.21		55.14	5.86	2.96	1.50	0.21
	26.55	5.58	2.95	1.18	0.37		48.36	4.12	2.96	1.62	0.22
	25.49	4.48	2.95	1.14	0.37		100.00	16.97	2.76	1.18	0.00
4	100.00	77.62	2.48	1.28	0.00	13	94.66	15.28	2.78	1.52	0.02
	46.61	28.15	2.74	1.22	0.27		73.95	9.95	2.85	1.11	0.09
	28.11	12.88	2.83	1.17	0.35		51.64	4.72	2.96	1.44	0.20
	18.32	7.52	2.96	1.05	0.48		45.92	3.41	2.97	1.10	0.21
	16.72	6.34	2.98	1.34	0.50		100.00	16.66	2.81	1.45	0.00
5	100.00	44.08	2.59	1.36	0.00	14	94.67	16.12	2.81	1.62	0.00
	68.41	26.51	2.70	1.22	0.11		79.11	10.57	2.89	1.56	0.08
	40.90	9.60	2.83	1.29	0.24		61.14	5.35	2.97	1.43	0.16
	29.71	6.54	2.94	1.33	0.35		55.01	4.32	2.98	1.49	0.18
	26.21	5.32	2.95	1.40	0.36		100.00	15.40	2.78	1.32	0.00
6	100.00	43.63	2.58	1.46	0.00	15	93.39	13.86	2.78	1.43	0.00
	69.91	22.94	2.72	1.31	0.14		71.08	9.18	2.85	1.31	0.07
	41.15	9.46	2.88	1.41	0.30		53.60	4.90	2.95	1.32	0.16
	30.44	5.62	2.95	1.40	0.36		48.98	4.25	2.96	1.23	0.18
	26.37	4.85	2.96	1.52	0.38		100.00	11.20	2.85	1.69	0.00
7	100.00	73.55	2.56	1.40	0.00	17	89.70	8.79	2.88	1.45	0.02
	60.01	34.41	2.69	1.31	0.13		84.80	7.82	2.89	1.48	0.04
	22.44	6.67	2.90	1.10	0.34		64.74	4.88	2.97	1.30	0.12
	19.51	5.32	2.95	1.34	0.40		58.64	3.79	2.98	1.39	0.13
9	100.00	18.57	2.78	1.19	0.00	19	100.00	6.55	2.86	0.89	0.00
	82.37	12.66	2.84	1.26	0.06		95.26	5.95	2.87	0.86	0.01
	64.92	6.62	2.91	1.26	0.13		87.57	4.74	2.89	0.80	0.03
	51.24	3.73	2.97	1.13	0.19		56.65	1.60	2.98	0.80	0.12
	49.35	3.36	2.97	1.03	0.19	54.60	1.55	2.97	0.83	0.11	

Views from left to right include T_2 spectra of different water saturation states of a representative rock sample of each pore structure type discussed in Section 3.1 (X: T_2 /ms, Y: porosity $S(T_2)$ /%), corresponding cumulative curves under different water saturation states and fitting models of micro-pores, enlarged view of cumulative curves of macro-pores (circled by the orange dotted square in middle view), and corresponding fitting models. T_{2cut} is plotted by the solid orange line. Figure 5A shows T_2 spectra, cumulative curves, and corresponding fitting models of both macro-pores (right view) and micro-pores (middle view) of No. 4 from Type A under different water saturation: 100% (black line); 6.61% (red line); 28.11% (blue line); 18.32% (pink line); 16.72% (green line). Figure 5B shows T_2 spectra, cumulative curves, and corresponding fitting models of both macro-pores (right view) and micro-pores (middle view) of No. 9 from Type B under different water saturation: 100% (black line); 82.37% (red line); 64.92% (blue line); 49.35% (green line). Figure 5C shows T_2 spectra, cumulative curves, and corresponding fitting models of both macro-pores (right view) and micro-pores (middle view) of No. 15 from Type C under different water saturation: 100% (black line); 93.39% (red line); 71.08% (blue line); 53.6% (pink line); 48.98% (green line). Figure 5D shows T_2 spectra, cumulative curves, and corresponding fitting models of both macro-pores (right view) and micro-pores (middle view) of No. 17 from Type D under different water saturation: 100% (black line); 89.7% (red line); 84.79% (blue line); 64.74% (pink line); 58.64% (green line). Figure 5E shows T_2 spectra, cumulative curves, and corresponding fitting models of both macro-pores (right view) and micro-pores (middle view) of No. 19 from Type E under different water saturation: 100% (black line); 95.26% (red line); 87.57% (blue line); 56.65% (pink line); 54.6% (green line).

The result shows that as S_w decreases, D_{va} increases, but D_{vb} has little variation. When S_w decreases to S_{wir} , D_{va} approximately equals 3. It also can be seen that as pore structure transferred from Type A to Type E, the maximum value of ΔD_{va} (the difference between D_{va} under S_{wir} state and that under 100% S_w state) becomes smaller.

The following two reasons have been explained: firstly, when large pores fill with gas, the residual water-saturated pores are still satisfied with the fractal theory, and variance of water saturation leads to the change of fractal dimension from NMR according to Equation (11). As water saturation variation is commonly caused by the volume change of movable water, while the immovable water seldom has changed; thus, water saturation variation results in the D_{va} change. Secondly, from Type A to Type E, as pore structure gets worse, immovable water content increases gradually, and movable water content decreases, the influence of water saturation on D_{va} decreases, responding to the decrease in ΔD_{va} .

Figure 6 shows the relationship between ΔD_{va} and S_w , and the relationship model is

$$\Delta D_{va} = D_{va,i} - D_{va,0} = -1.0101S_w + 0.40813S_w^2 + 0.60141 \quad (12)$$

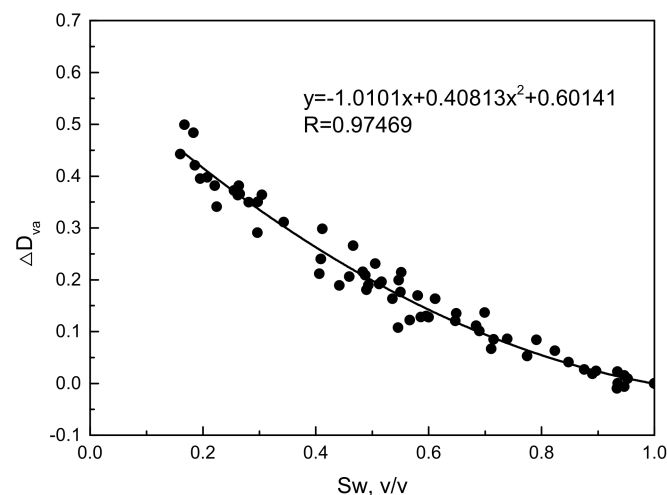


Figure 6. Relationship between ΔD_{va} and S_w .

The goodness of fit is 0.97469. As S_w is within the range of $[0, 1]$, ΔD_{va} is a monotonic increasing function of water saturation in Equation (12). Thus, the following water saturation prediction model is obtained:

$$S_w = 2.7955\Delta D_{va}^2 + 3.0032\Delta D_{va} + 0.9791 \quad (13)$$

4. Application

New methods are applied in the interval of 4385–4425 m in Well $\times 5$ in the Jidong field, belonging to the gas-bearing tight sandstone reservoir of the Shahejie formation [32,33]. In the study area, T_2 spectra are measured by CMR, and T_{2cut} value adopts 15 ms. According to T_2 spectra and T_{2cut} , parameters of successive depth, including the fractal dimension D_{va} and D_{vb} , irreducible porosity is obtained. As discussed above, gas bearing mainly has affection on macro-pores and leads to the variance of D_{va} . Thus, ΔD_{va} is the point to calculate water saturation S_w . To solve it, we have found that $D_{va,0}$ (D_{va} under 100% S_w state) has a positive relationship with Sw_{ir} , as discussed in Section 5.2. Then, $\Delta D_{va} = D_{va} - D_{va,0}$ can be calculated by Equation (14). Sw_{ir} is the ratio of NMR-derived irreducible porosity, and the density-derived total porosity, S_w , is calculated by Equation (13). Pore structure can be typed according to the projection of $(D_{va,0}, D_{vb})$ in Figure 4. The evaluation result is shown in Figure 7, and specific parameters of layers 1–9 are listed in Table 3.

$$D_{va,0} = 0.00781S_{wir} + 3.61315 \quad (14)$$

Table 3. Reservoir parameters of Layers 1–9.

Layer	RT (ohm.m)	POR (%)	PERM (md)	Sw_Archie (v/v)	Swir_nmr (v/v)	SW_T2 (v/v)	Dva0	Dvb	Dva	Type	Production
1	38	10.1	0.34	0.65	0.64	0.89	2.649	1.254	2.663	II	–
2	16	4.3	0.03	1	0.76	0.91	2.804	2.069	2.846	III/IV	–
3	31	11.2	0.87	0.69	0.55	0.58	2.594	0.875	2.733	I/III	–
4	30	13.2	1.6	0.6	0.37	0.48	2.429	0.954	2.638	I/II	–
5	41	10.7	0.45	0.65	0.41	0.51	2.558	1.104	2.699	I/II/IV	Gas 1.1×10^4 m ³ ,
6	31	10.2	0.22	0.64	0.5	0.53	2.646	2.288	2.702	I/II	no water
7	36	7.7	0.08	0.71	0.91	0.97	2.863	1.763	2.966	IV/V	–
8	31	6.5	0.01	1	0.8	0.83	2.75	1.085	2.797	IV/V	–
9	10	7.3	0.05	1	0.9	0.82	2.86	0.29	2.89	V	–

Tracks from left to right include Tracks 1–5: natural gamma-ray logging (GR: GAPI); depth (meters); geo-logging lithology; apparent resistivity logs (RLLD/RLLS: OHMM); acoustic-wave slowness logs (AC:us/m)/bulk density (DEN: g/cm³)/neutron porosity (CNL: %). Track 6: CMR T_2 spectra Track 7: T_2 calculated permeability (PERM: md). Track 8: the fractal dimension from NMR (DVA/DVB: none); DVA under 100% Sw state (DVA0:none). Track 9: irreducible water saturation (SWIR: v/v) calculated according to T_{2cut} /experimental data (dotted SWIR: v/v). Track 10: water saturation computed by the Archie model (SW: V/V)/experimental irreducible water saturation of rock samples (SWIR:V/V). Track 11: water saturation computed by the new method (SWT2: V/V)/experimental irreducible water saturation of rock samples (SWIR: V/V). Track 12: new method derived pore structure type (PORE_TPYE). Track 13: layer number.

In Figure 7, it can be seen that the pore structure classification result is consistent with geo-logging lithology and permeability calculated from T_2 spectra. The pore structure of shale recorded by geo-logging is classified into Type V by the new method. Furthermore, the permeability of the reservoir with pore structures of Types I and II (Layers 3–6) is higher than that with pore structures dominantly composed of Types IV and V (Layers 2,7–9). The result indicates that pore structure characterization and classification methods based on fractal analysis from NMR spectra can be used in quality reservoir prediction of tight sandstone.

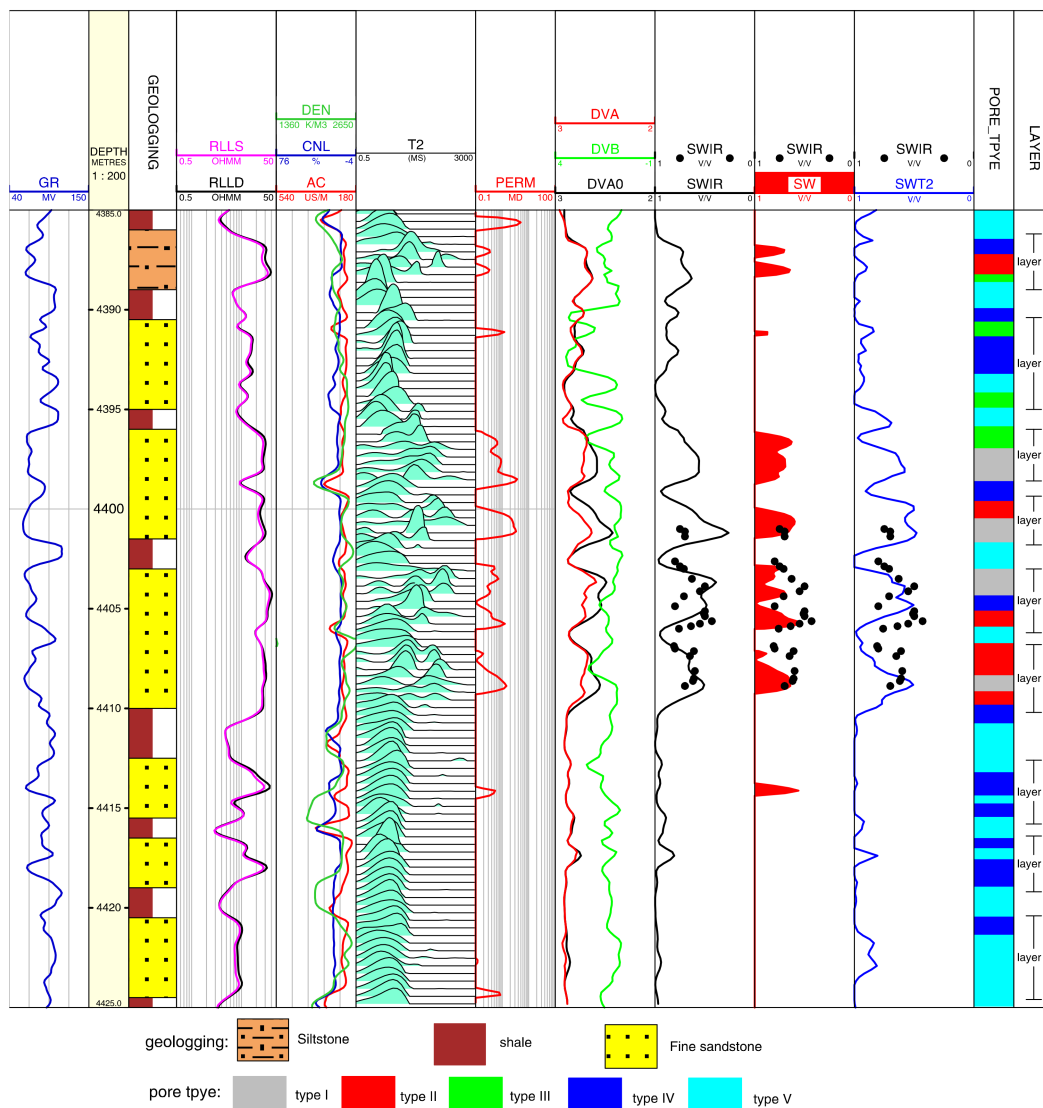


Figure 7. Evaluation result of new methods in Well x5.

It also can be seen that the calculated water saturation is in good agreement with experimental data, and its accuracy is improved than when calculated by the Archie model. For Layer 5–6, the calculated water saturation (SWT2) basically equals irreducible water saturation (SWIR); its production result is 1×10^4 m³ gas without water, which indicates that the water saturation prediction method based on fractal analysis from NMR spectra can be used in reservoir evaluation of tight sandstone.

5. Discussion and Future Work

5.1. Relationship of the Fractal Dimension from NMR with the Pore Size from the T₂ Spectrum

To analyze the relationship between the fractal dimension (D_{va} and D_{vb}) from NMR and the pore size from the T₂ spectrum, according to positions and ranges of the T₂ peak value of rock samples, the T₂ value is subdivided into five parts, corresponding to five ranges of pore size. Figure 8 shows the corresponding relationship between the T₂ spectrum and pore size. In Figure 8, f_1 (T₂ range of 70–900 ms), f_2 (T₂ range of 20–70 ms), f_3 (T₂ range of 5–20 ms), f_4 (T₂ range of 2–5 ms), and f_5 (T₂ range of 0.1–2 ms) are marked in grey, green, purple, orange, and blue, respectively. For 19 rock samples, the volume fraction of each pore size type is calculated and listed in Table 1.

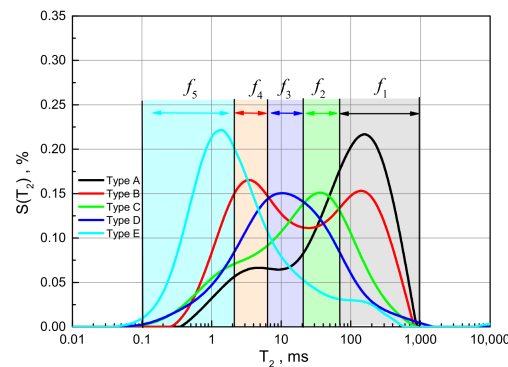


Figure 8. Corresponding relationship between T_2 spectra and pore space.

As discussed above, movable water dominantly resides in macro-pores, and immovable water mainly occupies micro-pores. According to the T_{2cut} range of 19 rock samples in Table 1, D_{va} has a relationship with f_1 and f_2 , and D_{vb} is the function of f_3 , f_4 , and f_5 . Relationships between the fractal dimension from NMR and volume fraction are shown in Equations (15) and (16):

$$D_{va} = 3.12844 - 0.7203f_1 - 0.7524f_2, R = 0.92278 \quad (15)$$

$$D_{vb} = 1.14533 + 2.7365f_3 - 1.3372f_4 - 1.6889f_5, R = 0.78624 \quad (16)$$

The result shows that the fractal dimension D_{va} is inversely proportional to f_1 and f_2 ; it indicates that increasing f_1 and f_2 , which are occupied by movable water leads to decreasing bound water content and fractal dimension D_{va} . Additionally, the fractal dimension D_{vb} is in inverse ratio to f_4 and f_5 , while it is in direct ratio to f_3 . In other words, increasing f_4 and f_5 results in decreasing fractal dimension D_{vb} , but increasing f_3 leads to increasing fractal dimension D_{vb} . Figure 9 shows the comparison between the fractal dimension derived from $\text{Log}_{10}S_v - \text{Log}_{10}T_2$ line slopes and the calculated fractal dimension by Equations (15) and (16). D_{va} and D_{vb} are marked in red and black, respectively. It can be seen that the goodness of fit is 0.92278 and 0.78624 for D_{va} and D_{vb} , indicating that pore structure characterization can be achieved based on fractal analysis of the NMR spectra.

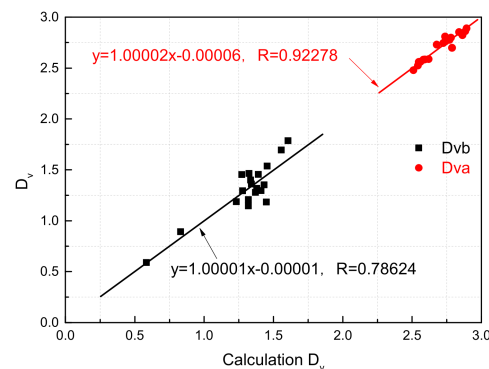


Figure 9. Comparison between the T_2 curve derived fractal dimension and the calculated fractal dimension by Equations (15) and (16).

5.2. Relationship of the Fractal Dimension from NMR with S_{wir} and T_{2lm}

Figures 10 and 11 show the relationship of the fractal dimension from NMR D_v (D_{va} colors red and D_{vb} colors black) of 19 water-saturated rock samples with irreducible water saturation S_{wir} and geometrical mean of the relaxation spectra T_{2lm} , respectively. Specific parameters are listed in Table 1. The result shows that D_{va} has a positive relationship with S_{wir} and T_{2lm} , while D_{vb} is unrelated to S_{wir} or T_{2lm} . Relationship models are

$$D_{va} = 0.00781S_{wir} + 3.61315 \quad (17)$$

$$D_{va} = 2.99586 + 0.5815T_{2lm}^{0.49308} \quad (18)$$

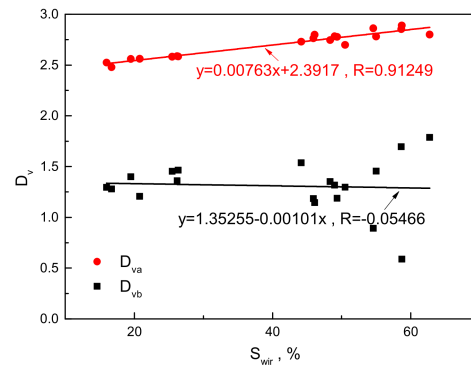


Figure 10. D_v — S_{wir} relationship (D_{va} , S_{wir}) and (D_{vb} , S_{wir}) are marked by red spot and black square, respectively.

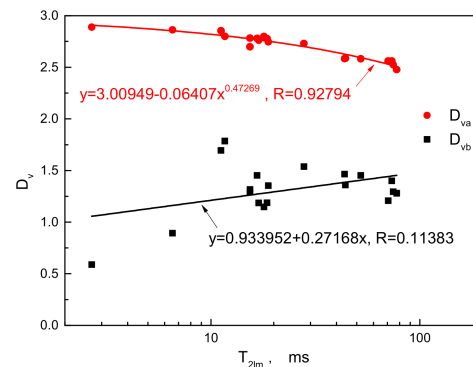


Figure 11. D_v — T_{2lm} relationship (D_{va} , T_{2lm}) and (D_{vb} , T_{2lm}) are marked by red spot and black square, respectively.

The goodness of fit of Equations (17) and (18) are 0.91249 and 0.92794, respectively.

The following reasons can explain it: T_{2lm} and S_{wir} are important reflection parameters of pore structure. In sandstone reservoirs, greater T_{2lm} and lower S_{wir} commonly represent a higher proportion of macro-pores, which indicate higher fluid flow capacity and more favorable pore structure. According to Equation (17), the fractal dimension D_{va} , mainly reflecting the characteristics of macro-pores, directly affects pore structure and fluid flow capacity. Thus, D_{va} is in direct ratio to T_{2lm} and S_{wir} . However, D_{vb} is a characteristic parameter of micro-pores, which are dominantly occupied by immovable water and have little contribution to pore structure or fluid flow capacity; thus, it has no obvious correlation with T_{2lm} and S_{wir} .

5.3. Fractal-Based Water Saturation Prediction Model from NMR

As discussed in Section 2.2, in the water-saturated rock, when macro-pores fill with gas, the residual water-saturated pores are still satisfied with fractal theory, and its fractal dimension from NMR decreases. Figure 6 and Equation (12) have illustrated the relationship between S_w and ΔD_{va} of 16 rock samples; the result indicates that for gas-bearing tight sandstone with different pore structures, S_w - ΔD_{va} relationship models are similar. The error in Figure 6 and Equation (12) mainly results from experimental data and T_2 spectrum inversion. In Figure 7, the water saturation calculated by Equation (13) is consistent with experimental water saturation. The error mainly results from the NMR signal-to-noise ratio, error of Equation (13), and error of irreducible water saturation calculated with a fixed T_{2cut} value.

5.4. Future Work

Further research directions and subjects concerning pore structure investigation and water saturation prediction methods for gas-bearing tight sandstone based on fractal analysis from NMR may be anticipated in the following:

- A. The fractal dimension of tight sandstone is closely related to its pore structure [34]. The pore structures in the different study areas have their specific fractal features and may be characterized by double [35], triple, or multi-fractals. Launching research to figure out fractal characteristics in a specific study area is necessary;
- B. The double fractal theory is the basis of the water saturation prediction method based on the fractal dimension from NMR proposed in this paper. In order to improve the accuracy, multi-fractal theory can be introduced to establish the water saturation prediction model;
- C. At present, 2D NMR logging is widely used in reservoir evaluation, and the research on fractal characteristics of 2D NMR is a new hot spot;
- D. For T_2 , the relaxation characteristics of oil-bearing sandstone differ greatly from that of gas-bearing sandstone [36]. The water saturation prediction model for gas-bearing sandstone proposed in this paper cannot be applied in oil-bearing sandstone reservoirs, but it still has reference and guiding significance for deriving a water saturation prediction model for oil-bearing sandstone;
- E. The multi-fractal theory has been widely applied in porous sandstone, describing fractal characteristics of pore space [37,38]. It can be further applied to carbonate and volcanic reservoirs;
- F. The T_{2cut} and T_{2lm} are very important parameters for our research results, and lots of factors have significant affection on their values, such as pore size, clay content, pressure, and others. Previous studies have proved that factors leading to the decrease in the T_{2cut} and T_{2lm} include the compressed rock matrix, the growth of clay content, and hydrocarbon limiting in micro-pores. In the extending application of the new method in various types of hydrocarbon-bearing reservoirs, it is necessary to conduct experiments and analysis on the influence factors on the T_{2cut} and T_{2lm} .

6. Conclusions

In this paper, we focus on the fractal characteristics of the pore size of tight sandstone from NMR. According to the double fractal theory and T_{2cut} value, the fractal dimension from NMR of both macro-pore system D_{va} and of micro-pore system D_{vb} are derived. In addition, the relationship of the fractal dimension from NMR with pore structure and water saturation is analyzed. Based on it, a pore structure characterization and classification method for water-saturated tight sandstone and a water saturation prediction method in a gas-bearing tight sandstone reservoir are proposed. The main conclusions are as follows:

- (1) Rock samples having similar pore structures have similar fractal features. The experimental data show that samples have a similar T_2 curve monography, although the porosity differs, and D_{va} and D_{vb} values are centrally distributed. This is the basis for pore structure characterization and classification method based on the fractal dimension from NMR. In addition, D_{va} is in direct ratio to T_{2lm} and S_{wir} , but D_{vb} has no obvious correlation with these two parameters;
- (2) To analyze the relationship between pore size and the fractal dimension from NMR, pore size is divided into five types according to T_2 spectra ranges, including f_1 (T_2 range of 70–900 ms), f_2 (T_2 range of 20–70 ms), f_3 (T_2 range of 5–20 ms), f_4 (T_2 range of 2–5 ms), and f_5 (T_2 range of 0.1–2 ms). The fractal dimension D_{va} is inversely proportional to f_1 and f_2 , increasing f_1 and f_2 , which are occupied by the movable water, leading to decreasing bound water content and fractal dimension D_{va} . The fractal dimension D_{vb} is in inverse ratio to f_4 and f_5 , while it is in direct ratio to f_3 , increasing f_4 and f_5 results in decreasing fractal dimension D_{vb} , but increasing f_3 leads to increasing fractal dimension D_{vb} ;

- (3) In water-saturated rock, when macro-pores fill with gas, residual water-saturated pores are still satisfied with the fractal theory. As the NMR signal of the gas-filling pores is too small to be measured, the fractal dimension from NMR changes. As S_w decreases, D_{va} increases, but D_{vb} has little variation, and ΔD_{va} (the increment of D_{va}) is directly related to the water saturation of gas-bearing tight sandstone. When S_w decreases to S_{wir} , D_{va} approximately equals 3. As the pore structure transferred from Type A to Type E, the maximum value of ΔD_{va} (the difference between D_{va} under S_{wir} state and that under 100% S_w state) becomes smaller;
- (4) Experimental data and application result show that firstly, pore structure evaluation and classification can be achieved based on fractal analysis from NMR spectra; the method can be further applied in reservoir quality evaluation and favorable reservoir prediction. Secondly, the accuracy of calculated water saturation by the new method is higher than that calculated by the Archie model, and the fractal-based water saturation prediction method from NMR extends the application area of NMR logging and also provides a non-electrical idea for the qualitative identification and evaluation of gas-bearing tight sandstone reservoir, it has a reference for the gas-bearing recognition of tight sandstone and carbonate reservoirs.

Author Contributions: Conceptualization and methodology, W.X. and Q.Y.; software, W.X.; validation, J.Z.; investigation, P.Z.; data curation, C.F.; writing—original draft preparation, W.X. and Q.Y.; writing—review and editing, G.W. All authors have read and agreed to the published version of the manuscript.

Funding: This article was supported by the National Natural Science Foundation of China (No. 41872133), the Research Foundation of China University of Petroleum-Beijing at Karamay (No. XQZX20230012) and the “Tianchi Talent” Introduction Plan Foundation of Xinjiang, China.

Data Availability Statement: Most of the data has been disclosed in the manuscript data table; other data cannot be disclosed due to confidentiality and can be obtained from the author (gareth123@126.com).

Conflicts of Interest: The authors declared that they have no conflict of interest in this work. We declare that we do not have any commercial or associative interest that represents a conflict of interest in connection with the work submitted.

References

1. Yan, S.O.N.G.; Zhuo, L.I.; Jiang, Z.; Qun, L.; Dongdong, L.; Zhiye, G. Progress and development trend of unconventional oil and gas geological research. *Pet. Explor. Dev.* **2017**, *44*, 675–685.
2. Ren, J.; Zhang, L.; Ezekiel, J.; Ren, S.; Meng, S. Reservoir characteristics and productivity analysis of tight sand gas in Upper Paleozoic Ordos Basin China. *J. Nat. Gas Sci. Eng.* **2014**, *19*, 244–250. [[CrossRef](#)]
3. Muther, T.; Nizamani, A.A.; Ismail, A.R. Analysis on the effect of different fracture geometries on the productivity of tight gas reservoirs Malays. *J. Fundam. Appl. Sci.* **2020**, *16*, 201–211. [[CrossRef](#)]
4. Lai, J.; Wang, G.; Wang, Z.; Chen, J.; Pang, X.; Wang, S.; Zhou, Z.; He, Z.; Qin, Z.; Fan, X. A review on pore structure characterization in tight sandstones. *Earth-Sci. Rev.* **2018**, *177*, 436–457. [[CrossRef](#)]
5. Xiao, D.; Lu, S.; Lu, Z.; Huang, W.; Gu, M. Combining nuclear magnetic resonance and rate-controlled porosimetry to probe the pore-throat structure of tight sandstones. *Pet. Explor. Dev.* **2016**, *43*, 1049–1059. [[CrossRef](#)]
6. Wang, R.; Shi, W.; Xie, X.; Zhang, W.; Qin, S.; Liu, K.; Busbey, A.B. Clay mineral content, type, and their effects on pore throat structure and reservoir properties: Insight from the Permian tight sandstones in the Hangjinqi area, north Ordos Basin, China. *Mar. Pet. Geol.* **2020**, *115*, 104281. [[CrossRef](#)]
7. Mandelbrot, B.B. *The Fractal Geometry of Nature*; Freeman: San Francisco, CA, USA, 1982.
8. Wang, F.; Yang, K.; Cai, J. Fractal characterization of tight oil reservoir pore structure using nuclear magnetic resonance and mercury intrusion porosimetry. *Fractals* **2018**, *26*, 1840017. [[CrossRef](#)]
9. Miao, T.; Yu, B.; Duan, Y.; Fang, Q. A fractal analysis of permeability for fractured rocks. *Int. J. Heat Mass Transf.* **2015**, *81*, 75–80. [[CrossRef](#)]
10. Jafari, A.; Babadagli, T. Estimation of equivalent fracture network permeability using fractal statistical network properties. *J. Pet. Sci. Eng.* **2012**, *92*, 110–123. [[CrossRef](#)]
11. Li, K. Analytical derivation of Brooks–Corey type capillary pressure models using fractal geometry and evaluation of rock heterogeneity. *J. Pet. Sci. Eng.* **2010**, *73*, 20–26. [[CrossRef](#)]
12. Li, X.; Chen, S.; Wang, X.; Zhu, Y.; Chang, M.; Uwamahoro, C. Pore structure heterogeneity of the Xiamaling Formation shale gas reservoir in the Yanshan area of China: Evaluation of geological controlling factors. *Acta Geol. Sin.-Engl. Ed.* **2019**, *93*, 588–603. [[CrossRef](#)]

13. Wang, Q.; Hu, Y.; Zhao, J.; Ren, L.; Zhao, C.; Zhao, J. Multiscale apparent permeability model of shale nanopores based on fractal theory. *Energies* **2019**, *12*, 3381. [[CrossRef](#)]
14. Li, B.; Liu, R.; Jiang, Y. A multiple fractal model for estimating permeability of dual-porosity media. *J. Hydrol.* **2016**, *540*, 659–669. [[CrossRef](#)]
15. Song, Z.; Liu, G.; Yang, W.; Zou, H.; Sun, M.; Wang, X. Multi-fractal distribution analysis for pore structure characterization of tight sandstone—A case study of the Upper Paleozoic tight formations in the Longdong District, Ordos Basin. *Mar. Pet. Geol.* **2018**, *92*, 842–854. [[CrossRef](#)]
16. Guo, X.; Huang, Z.; Zhao, L.; Han, W.; Ding, C.; Sun, X.; Yan, R.; Zhang, T.; Yang, X.; Wang, R. Pore structure and multi-fractal analysis of tight sandstone using MIP, NMR and NMRC methods: A case study from the Kuqa depression, China. *J. Pet. Sci. Eng.* **2019**, *178*, 544–558. [[CrossRef](#)]
17. Rembert, F.; Jougnot, D.; Guarracino, L. A fractal model for the electrical conductivity of water-saturated porous media during mineral precipitation-dissolution processes. *Adv. Water Resour.* **2020**, *145*, 103742. [[CrossRef](#)]
18. Feng, C.; Han, C.; Duan, W.; Wang, W.; Zhong, Y.; Feng, Z.; Zhang, N. Estimation of the Resistivity Index via Nuclear Magnetic Resonance Log Data Based on Fractal Theory. *Geofluids* **2020**, *2020*, 8871096. [[CrossRef](#)]
19. Shi, Y.; Meng, H.; Liu, T.; Zhang, H.; Wang, C. Evaluation of Relative Permeability From Resistivity Data for Fractal Porous Media. *Petrophys.-SPWLA J. Form. Eval. Reserv. Descr.* **2020**, *61*, 303–317. [[CrossRef](#)]
20. Karimpouli, S.; Tahmasebi, P. 3D multi-fractal analysis of porous media using 3D digital images: Considerations for heterogeneity evaluation. *Geophys. Prospect.* **2019**, *67*, 1082–1093. [[CrossRef](#)]
21. Zhao, P.; Luo, M.; Li, D.; Wu, Y.; Mao, Z.; Ostadhassan, M. Fractal Characterization and Petrophysical Analysis of 3D Dynamic Digital Rocks of Sandstone. *Petrophys.-SPWLA J. Form. Eval. Reserv. Descr.* **2021**, *62*, 500–515. [[CrossRef](#)]
22. Zhou, S.; Liu, D.; Cai, Y.; Yao, Y. Fractal characterization of pore–fracture in low-rank coals using a low-field NMR relaxation method. *Fuel* **2016**, *181*, 218–226. [[CrossRef](#)]
23. Liu, X.; Jin, Z.; Lai, J.; Fan, X.; Guan, M.; Shu, H.; Wang, G.; Liu, M.; Luo, Y. Fractal behaviors of NMR saturated and centrifugal T₂ spectra in oil shale reservoirs: The Paleogene Funing formation in Subei basin, China. *Mar. Pet. Geol.* **2021**, *129*, 105069. [[CrossRef](#)]
24. Zhao, X.; Yang, Z.; Lin, W.; Xiong, S.; Luo, Y.; Liu, X.; Xia, D. Fractal study on pore structure of tight sandstone based on full-scale map. *Int. J. Oil Gas Coal Technol.* **2019**, *22*, 123–139. [[CrossRef](#)]
25. Wang, J.; Jiang, F.; Zhang, C.; Song, Z.; Mo, W. Study on the Pore Structure and Fractal Dimension of Tight Sandstone in Coal Measures. *Energy Fuels* **2021**, *35*, 3887–3898. [[CrossRef](#)]
26. Xie, W.; Yin, Q.; Wang, G.; Yu, Z. Variable dimension fractal-based conversion method between the nuclear magnetic resonance T₂ spectrum and capillary pressure curve. *Energy Fuels* **2020**, *35*, 351–357. [[CrossRef](#)]
27. Wei, W.; Cai, J.; Hu, X.; Han, Q. An electrical conductivity model for fractal porous media. *Geophys. Res. Lett.* **2015**, *42*, 4833–4840. [[CrossRef](#)]
28. Wang, F.; Cai, J. Characterization of petrophysical properties in tight sandstone reservoirs. In *Petrophysical Characterization and Fluids Transport in Unconventional Reservoirs*; Elsevier: Amsterdam, The Netherlands, 2019; pp. 37–59.
29. Kashif, M.; Cao, Y.; Yuan, G.; Asif, M.; Javed, K.; Mendez, J.N.; Khan, D.; Miruo, L. Pore size distribution, their geometry and connectivity in deeply buried Paleogene Es1 sandstone reservoir, Nanpu Sag, East China. *Pet. Sci.* **2019**, *16*, 981–1000. [[CrossRef](#)]
30. Zheng, H.J.; Dong, Y.X.; Zhu, G.Y.; Wang, X.D.; Xiong, Y. High-quality source rocks in Nanpu Sag. *Pet. Explor. Dev.* **2007**, *34*, 385.
31. Guo, Y.; Pang, X.; Dong, Y.; Jiang, Z.; Chen, D.; Jiang, F. Hydrocarbon generation and migration in the Nanpu Sag, Bohai Bay Basin, eastern China: Insight from basin and petroleum system modeling. *J. Asian Earth Sci.* **2013**, *77*, 140–150. [[CrossRef](#)]
32. Wang, E.; Liu, G.; Pang, X.; Wu, Z.; Li, C.; Bai, H.; Zhang, Z. Sedimentology, diagenetic evolution, and sweet spot prediction of tight sandstone reservoirs: A case study of the third member of the Upper Paleogene Shahejie Formation, Nanpu Sag, Bohai Bay Basin, China. *J. Pet. Sci. Eng.* **2020**, *186*, 106718. [[CrossRef](#)]
33. Xie, W.; Yin, Q.; Wang, G.; Guan, W.; Yu, Z. Modeling of gas saturation based on acoustic wave and pore structure classification and application in the low-porosity and low-permeability reservoir. *Arab. J. Geosci.* **2021**, *14*, 917. [[CrossRef](#)]
34. Wu, B.; Xie, R.; Wang, X.; Wang, T.; Yue, W. Characterization of pore structure of tight sandstone reservoirs based on fractal analysis of NMR echo data. *J. Nat. Gas Sci. Eng.* **2020**, *81*, 103483. [[CrossRef](#)]
35. Sun, W.; Liu, C.; Wang, Y.; Bai, L.; Li, W.; Li, S. A practical method to construct capillary pressure curves of reservoir using nmr logging date. *Int. J. Oil Gas Coal Technol.* **2019**, *22*, 433–446. [[CrossRef](#)]
36. Winkler, M.; Freeman, J.J.; Appel, M. The limits of fluid property correlations used in NMR well logging: An experimental study of reservoir fluids at reservoir conditions. *Petrophys.-SPWLA J. Form. Eval. Reserv. Descr.* **2005**, *46*.
37. Nie, R.S.; Zhou, J.; Chen, Z.; Liu, J.; Pan, Y. Pore structure characterization of tight sandstones via a novel integrated method: A case study of the Sulige gas field, Ordos Basin (Northern China). *J. Asian Earth Sci.* **2021**, *213*, 104739. [[CrossRef](#)]
38. Ge, X.; Fan, Y.; Zhu, X.; Chen, Y.; Li, R. Determination of nuclear magnetic resonance t₂ cutoff value based on multifractal theory—An application in sandstone with complex pore structure. *Geophysics* **2015**, *80*, D11–D21. [[CrossRef](#)]

Disclaimer/Publisher’s Note: The statements, opinions and data contained in all publications are solely those of the individual author(s) and contributor(s) and not of MDPI and/or the editor(s). MDPI and/or the editor(s) disclaim responsibility for any injury to people or property resulting from any ideas, methods, instructions or products referred to in the content.